

Fermi-bubble bulk and edge analysis reveals dust, cooling breaks and cosmic-ray diffusion, facilitating a self-consistent model

URI KESHET,¹ ILYA GURWICH,^{2,3} ASSAF LAVI,¹ DINA AVITAN,⁴ AND TEODOR LINNIK⁴

¹*Physics Department, Ben-Gurion University of the Negev, POB 653, Be'er-Sheva 84105, Israel*

²*Qedma Quantum Computing, Tel-Aviv, Israel*

³*Physics Department, NRCN, POB 9001, Be'er-Sheva 84190, Israel*

⁴*Computer Science Department, Ben-Gurion University of the Negev, POB 653, Be'er-Sheva 84105, Israel*

ABSTRACT

The full, radio to γ -ray spectrum of the Fermi bubbles is shown to be consistent with standard strong-shock electron acceleration at the bubble edge, without the unnatural energy cutoffs and unrealistic electron cooling of previous studies, if the ambient interstellar radiation is strong; the γ -ray cooling break should then have a microwave counterpart, undetected until now. Indeed, a broadband bubble-edge analysis uncovers a pronounced downstream dust component, which masked the anticipated ~ 35 GHz spectral break, and the same overall radio softening consistent with Kraichnan diffusion previously reported in γ -rays. A self-consistent bulk and edge model implies a few Myr-old bubbles, with fairly uniform radiation fields and enhanced magnetization near the edge.

1. Introduction

The bipolar Fermi bubbles (FBs), emanating from the center of the Milky Way (Baganoff et al. 2003; Bland-Hawthorn & Cohen 2003) and extending out to $|b| \gtrsim 50^\circ$ latitudes, each presents as a fairly uniform γ -ray lobe (Dobler et al. 2010; Su et al. 2010), demarked by an X-ray shell (Keshet & Gurwich 2018), and coincident with microwave emission (Dobler 2012a; Planck Collaboration 2013) which brightens to a haze (Finkbeiner 2004) near the Galactic center. Their morphology, X-ray shells (Keshet & Gurwich 2018), and bulk (volume-integrated; Su et al. 2010; Dobler 2012b; Huang et al. 2013; Hooper & Slatyer 2013; Ackermann et al. 2014) and edge (Keshet & Gurwich 2017) energy spectra indicate that the FBs arose a few Myr ago as super-massive black hole (SMBH) energy injection, which must have been collimated (Mondal et al. 2022) and nearly perpendicular to the Galactic plane (Sarkar et al. 2023). The resulting outflows drove strong, Mach $\gtrsim 5$ forward shocks (Keshet & Gurwich 2017), preferentially heating the ions, which remain largely non-equilibrated with the electrons (Keshet & Gurwich 2018).

These collisionless shocks were found to accelerate a flat, $p \equiv -d \ln n / d \ln E \simeq 2.1$ energy spectrum of cosmic-ray (CR) electrons (CREs) (Dobler 2012b;

Planck Collaboration 2013), which subsequently undergo Kraichnan-like (Kraichnan 1965; Berezhinskii et al. 1990) diffusion of coefficient $D \propto E^{1/2}$ downstream (Keshet & Gurwich 2017). Despite considerable research, the sub-X-ray diffuse spectrum was characterized only in a narrow, 20–60 GHz band, and the γ -ray spectrum was modelled non-self-consistently, invoking in particular unnaturally low, ~ 1 –10 TeV CR cutoffs (*cf.* Sherf et al. 2017) to explain the observed $\epsilon \sim 50$ GeV photon break. In addition, hadronic models show a $E < 1$ GeV spectrum harder than observed, whereas present leptonic models do not consistently model CRE cooling, invoking a power-law spectrum extending to very high energies corresponding to unrealistically young bubbles (Crocker & Aharonian 2011; Fujita et al. 2013; Yang et al. 2013; Ackermann et al. 2014).

Figure 1 shows the specific I_ϵ γ -ray and I_ν microwave intensities, where ϵ and ν are the photon energy and frequency. The above arguments indicate that the γ -rays arise from the inverse-Compton (IC) scattering of the ambient radiation field by the CREs. Starlight photons of mean $\epsilon \simeq 1$ eV energy¹ dominate the interstellar radiation budget above the Galactic center, out to a height of at least 5 kpc (*e.g.*, Ackermann et al. 2014; Popescu et al. 2017). The massive FB-driven outflows, not incorporated in typical radiation models

keshet.uri@gmail.com

¹ We use ϵ for seed photons and ϵ for up-scattered photons.

(which may underestimate starlight even near the Galactic center; *e.g.*, Ajello et al. 2016), have likely elevated the starlight and infrared energy densities considerably, out to the ~ 10 kpc height of the bubbles, by removing much of the ambient absorbers. Hence, the $\epsilon \sim 50$ GeV break is naturally explained as the $\epsilon \simeq 3(m_e c^2)^2/16\epsilon \simeq 50\epsilon_1^{-1}$ GeV, Klein-Nishina (KN; *e.g.*, Rybicki & Lightman 1979) suppression of IC-scattered starlight, whereas the $\epsilon \gtrsim$ few GeV softening is shown below to be the signature of a cooling break. Here, m_e is the electron mass, c is the speed of light, and $\epsilon_1 \equiv \epsilon/1$ eV. In such a model, the ~ 50 GeV break should become less pronounced at higher latitudes, where it is increasingly washed out by the spectrally-flat, IC-scattered cosmic microwave background (CMB) photons; indeed, such a trend is hinted by spatially resolved (Hooper & Slatyer 2013) and edge (Keshet & Gurwich 2017) FB spectra.

2. Leptonic model

We assume that CREs are injected at the shock with index $p \simeq (r+2)/(r-1)$, thought to depend only on the shock compression ratio r (Axford et al. 1977; Krymskii 1977; Bell 1978; Blandford & Ostriker 1978) if scattering is sufficiently isotropic (Keshet et al. 2020), implying a shock velocity

$$v \simeq \sqrt{\frac{2(p+2)\Gamma k_B T_u}{(2p+1-3\Gamma)m}} \simeq 1500 \sqrt{\frac{T_{0.2}}{q}} \text{ km s}^{-1}. \quad (1)$$

Here, $m \simeq 0.59m_p$ and m_p are the mean and proton masses, $T_u \equiv 0.2T_{0.2}$ keV/ k_B (Miller & Bregman 2013; Kataoka et al. 2013; Keshet & Gurwich 2018) is the upstream temperature, k_B is Boltzmann's constant, and we adopted an adiabatic index $\Gamma = 5/3$ in the last, $p \simeq 2.1$ approximation where $q \equiv (p-2)/0.1$ approaches unity. Such a $p \simeq 2.1$ spectrum reproduces the hard synchrotron fit in Fig. 1 for non-cooled CREs, and the flat ~ 3 –30 GeV spectrum for cooled CREs. The FB age for a simple, $R \propto t^{2/3}$ Primakoff scaling (Courant & Friedrichs 1948; Keller 1956; Bernstein & Book 1980) of the $R \equiv 10R_{10}$ kpc FB height is then (Keshet & Gurwich 2018)

$$t \simeq \frac{2R}{3v} \simeq 4.4R_{10} \sqrt{\frac{q}{T_{0.2}}} \text{ Myr}. \quad (2)$$

FB CREs cool by synchrotron and IC emission, thus softening to an index $p+1$ above the cooling-break energy

$$E_b \simeq \frac{3m_e^2 c^3}{4\sigma_T t u} \approx 35 u_3^{-1} t_3^{-1} \text{ GeV}, \quad (3)$$

implying a synchrotron break at frequency

$$\nu_b \simeq \frac{3Bem_e c}{8\pi(\sigma_T t u)^2} \simeq 51 u_3^{-2} t_3^{-2} B_3 \text{ GHz}, \quad (4)$$

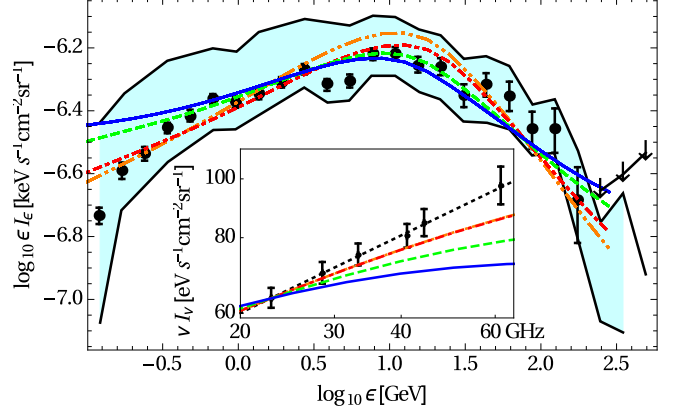


Figure 1. Bulk γ -ray (Ackermann et al. 2014) and (inset) microwave (Planck Collaboration 2013) FB spectra (black statistical error bars and upper-limit arrows, with cyan-shaded systematic uncertainty), synchrotron power-law fit ($I_\nu \propto \nu^{-0.57 \pm 0.06}$; dotted black curve), and one-zone leptonic models with $p = 2.1$, $u_i = 0.1 \text{ eV cm}^{-3}$, and additional parameters (with an increasing starlight intensity) $\{u_s \text{ cm}^3/\text{eV}, t/\text{Myr}, B/\mu\text{G}\} = \{0.5, 10, 1.45\}$ (solid blue), $\{1, 5, 2\}$ (dashed green), $\{2, 2.4, 2.7\}$ (dot-dashed red), and $\{3, 1.8, 3.1\}$ (double-dot-dashed orange).

and an IC-scattered starlight break at energy

$$\epsilon_b \simeq \frac{3\epsilon}{4} \left(\frac{m_e c}{\sigma_T t u} \right)^2 \simeq 6.1 u_3^{-2} t_3^{-2} \epsilon_1 \text{ GeV}, \quad (5)$$

where the energy density

$$u \simeq u_s + u_i + u_c + \frac{B^2}{8\pi} \equiv 3u_3 \text{ eV cm}^{-3} \quad (6)$$

accounts respectively for the ambient $\epsilon_s \simeq 1$ eV starlight, $\epsilon_i \simeq 10^{-2}$ eV infrared (*e.g.*, Ackermann et al. 2014), $\epsilon_c \simeq 10^{-3}$ eV CMB, and magnetic, components. Here, $t_3 \equiv t/3$ Myr, $B_3 \equiv B/3\mu\text{G}$ is the normalized magnetic field, e is the electron charge, and σ_T is the Thomson cross-section. The ratio between synchrotron emissivity at frequency ν from a non-cooled, $n \propto E^{-p}$ CRE distribution, and starlight-IC emissivity at energy ϵ from the cooled CREs, is

$$\Phi \equiv \frac{\nu j_\nu}{\epsilon j_\epsilon} \simeq \phi(p) m_e^{-\frac{p+3}{2}} e^{\frac{p+5}{2}} c^{-\frac{p+7}{2}} \frac{u t}{u_s} B^{\frac{p+1}{2}} \nu^{\frac{3-p}{2}} \left(\frac{\epsilon}{\epsilon_1} \right)^{\frac{p-2}{2}} \\ \simeq 0.043 \frac{u}{u_s} t_3 B_3^{\frac{p+1}{2}} \nu_{10}^{\frac{3-p}{2}} \left(\frac{\epsilon_{10}}{0.46\epsilon_1} \right)^{\frac{p-2}{2}}, \quad (7)$$

where we defined $\nu_{10} \equiv \nu/10$ GHz and $\epsilon_{10} \equiv \epsilon/10$ GeV; the dimensionless function $\phi(p)$ is given in Appendix §A. Adopting the $u_i + u_c \ll u_s$ limit (henceforth), the ratio between radio and $\gtrsim 10$ GeV γ -ray intensities should approximately be given by Eq. (7).

FB observations indicate a fairly uniform CR distribution within the bubbles (Su et al. 2010; Ackermann et al.

2014), so t , B , u , and u_s can be determined in a one-zone approximation from Eqs. (4)–(7), given p , ε , ν_b , ϵ_b , and Φ measurements. An $\alpha \equiv d \ln j_\nu / d \ln \nu \simeq -0.55$ bulk microwave spectral index extending out to $\gtrsim 60$ GHz (Planck Collaboration 2013, and Fig. 1) implies that $p = 1 - 2\alpha \simeq 2.1$. Hence, the bulk and edge γ -ray spectra (Su et al. 2010; Ackermann et al. 2014; Keshet & Gurwich 2017) are consistent with an $\epsilon_b \equiv 3\epsilon_{b,3}$ GeV $\simeq 3$ GeV cooling break, we may use the observed ratio $\Phi \equiv 0.1\Phi_{0.1} \simeq 0.12$ between (henceforth) the $\epsilon = 10$ GeV (Ackermann et al. 2014) and $\nu = 23$ GHz (Planck Collaboration 2013) fluxes, and, taken at face value, $\nu_b > 60$ GHz. Equations (5)–(7) then yield the plausible $u_3 t_3 \simeq 1.4(\varepsilon_1/\epsilon_{b,3})^{1/2}$, $t_3 B_3^{1.55} \simeq 1.5\varepsilon_1^{0.05}\Phi_{0.1}u_s/u$, and $u_s/u \simeq 1 - 0.074B_3^2 u_3^{-1}$. However, the putative lower ν_b limit would then lead, via Eq. (4), to the unrealistic inequalities $B_3 \gtrsim 2.4\epsilon_{b,3}^{-1}\varepsilon_1$, $t_3 \lesssim 0.40\varepsilon_1^{-3/2}\epsilon_{b,3}^{1.55}\Phi_{0.1}u_s/u$, and $u_s \gtrsim 10\varepsilon_1^2\epsilon_{b,3}^{-2.05}\Phi_{0.1}^{-1}$ eV cm $^{-3}$.

3. Missing microwave cooling break

As the FBs cannot be basked in so much starlight, and are unlikely to be so young, the model is plausible only in the presence of a $\nu_b < 60$ GHz cooling break, unidentified until now due to an additional microwave component, most likely dust. Indeed, replacing the spectral break Eq. (4) by the hydrodynamic Eq. (2) fixes the model parameters $^2 t \simeq 4.4R_{10}(q/T_{0.2})^{1/2}$ Myr, $u \simeq 2.9R_{10}^{-1}(T_{0.2}\varepsilon_1/\epsilon_{b,3}q)^{1/2}$ eV cm $^{-3}$, and $B \simeq 3.1(T_{0.2}/q)^{Q/3}(\Phi_{0.1}u_s/R_{10}u)^{2Q/3}\mu\text{G}$, where we defined $Q \equiv (1 + q/30)^{-1} \simeq 1$. Equation (4) then predicts a spectral break at frequency

$$\nu_b \simeq 26 \frac{\epsilon_{b,3}}{\varepsilon_1} \left(\frac{T_{0.2}}{q} \right)^{Q/3} \left(\frac{\Phi_{0.1}u_s}{R_{10}u} \right)^{2Q/3} \text{ GHz}. \quad (8)$$

Figure 1 demonstrates a few one-zone leptonic-model fits to the bulk γ -ray spectrum, constrained also by the $\nu \simeq 23$ GHz *WMAP* data point. Here, we fix $p = 2.1$ and $u_i = 0.1$ eV cm $^{-3}$, and vary the other parameters; additional model fits are provided in Appendix §A. Interestingly, for the best-fit parameters, we find that the cooling break and KN turnaround approximately merge to yield a stronger spectral break. While the $u_s = 0.5$ eV cm $^{-3}$ fit marginally agrees, within statistical and systematic uncertainties, with the γ -ray data, much better fits are obtained for 1 eV cm $^{-3} \lesssim u_s \lesssim 3$ eV cm $^{-3}$. Such starlight energy densities are higher than usually assumed at $R \gtrsim 4$ kpc heights, but are plausible as the mean starlight inside the FB outflows, given conservative $u_s(R = 2 \text{ kpc}) \simeq 1.4$ eV cm $^{-3}$ estimates (Acker-

mann et al. 2014), as discussed above and in §6. For such u_s values, the γ -ray fit is surprisingly good, considering the oversimplified, one-zone approximation, and can be arbitrarily improved if this assumption is relaxed. In contrast, the microwave fit is poor in all our successful γ -ray models, as they require a $\nu_b < 40$ GHz cooling break. These quantitative conclusions are in line with the above qualitative estimates, and are not sensitive to our assumptions; in particular, we obtain similar results for different $2.0 \leq p \lesssim 2.2$ CRE spectra, different $u_i < 0.2u_s$ prescriptions, and two-zone models. For $p \gtrsim 2.3$, the γ -ray spectral fit becomes unacceptable for plausible t and u_s values, as shown in Appendix §A.

4. Bubble-edge analysis

Next, we analyze the FB edges, identified by gradient filters (Keshet & Gurwich 2017), and bin the data parallel to the edge in the same method used to measure the γ -ray (Keshet & Gurwich 2017) and X-ray (Keshet & Gurwich 2018) spectra in the near downstream. Here, we study lower frequencies, ranging from 45 MHz radio to 60 μm infrared, focusing in particular on cleaned microwave *WMAP* and *Planck* maps with point sources masked and the CMB subtracted, as described in Appendix §B. Figure 2 demonstrates (RGB colors) the γ -ray, infrared, and microwave sky in and around the FBs, and outlines (white contours) the north and south sectors used in our analysis. These sectors, crossing the FB edge at the top of each bubble, were chosen to contain large upstream and downstream regions with minimal extended contamination.

Figure 3 presents the spectrum of the downstream regions of both north (upper panels) and south (bottom panels) FBs, obtained by binning the data parallel to the edge and subtracting the upstream-based foreground and background (henceforth foreground). The spatial distribution is demonstrated (left panels) for select channels, all found to sharply brighten as one crosses downstream, facilitating a measurement of the spectrum (right panels) at different outward-oriented angular distances ψ from the edge. While the signal strengthens downstream with increasing $|\psi|$, the spectral shape is found to be robust as a function of ψ , and quite similar in the north and south bubbles, substantiating the validity of the measurement. As expected from previous studies, the north bubble shows more surrounding substructure, both upstream (Loop-I) and downstream (mainly at low frequencies); it also presents a more gradual γ -ray jump, possibly attributed in part to edge misalignment.

The cleaner, south bubble provides a good measurement of the synchrotron signal, found for the first time to persist down to frequencies as low as 45 MHz. In the

² We neglect a weak, $\varepsilon_1^{q/(30+q)}$ dependence of B and ν_b .

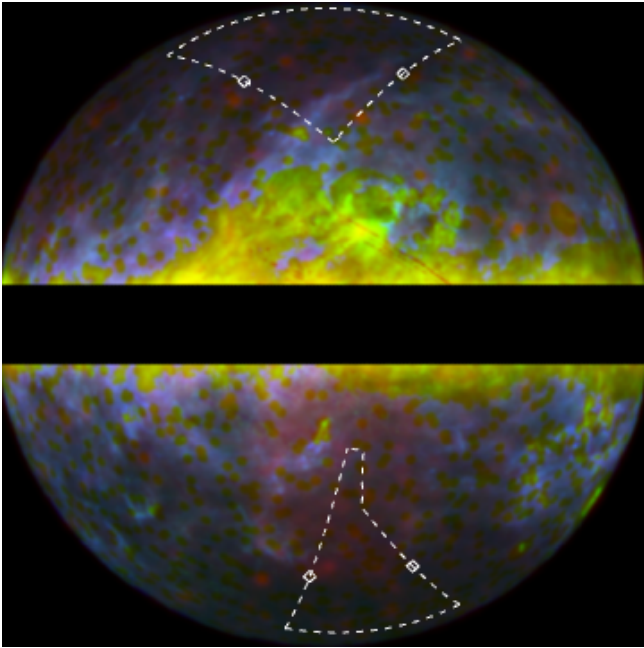


Figure 2. False-color image combining *Fermi*-LAT 30 GeV (red; see Appendix §C), *AKARI*-FIS WideL 140 μm (green; Doi et al. 2015), and *Planck* 143 GHz (blue) in an orthographic projection; the bright, $|b| \lesssim 5^\circ$ Galactic plane was masked. Our north and south sectors are highlighted (dashed white boundaries with diamonds where they intersect the FB edges).

present method, the spectral index can be accurately determined to be $\alpha = -0.77 \pm 0.03$ downstream (see Table 1). This index is softer by an $\eta = 0.20 \pm 0.07$ offset with respect to the $\alpha = -0.57 \pm 0.06$ bulk synchrotron index (Fig. 1), consistent with both Kraichnan and Kolmogorov diffusion of escaping CREs. A similar but slightly stronger softening was identified in the IC γ -ray emission from the edge, and was interpreted as arising from CRE diffusion (Keshet & Gurwicz 2017); its detection in radio validates this diffusive model.

A pronounced hard signal is found to dominate the downstream spectrum above ~ 100 GHz, extending up to an exponential turnaround in the infrared. The signal is well-fitted by an $I_\nu \propto \nu^{7/2}/(e^{h\nu/k_B T} - 1)$ spectrum (solid curves in Fig. 3), and is thus identified as thermal dust emission, of temperature $T \simeq 29 \pm 1$ K (33 ± 1 K) in the north (south) FB (see Table 1). Such temperatures, already hinted by coincident hot dust regions in *Planck* maps, may underestimate the true postshock T due to the inaccurate subtraction of $\lesssim 20$ K (*Planck* Collaboration et al. 2016) foreground dust. As the left panels of Fig. 3 show, the radial profiles of dust emission are nearly identical to those of IC and especially synchrotron emission, in both bubbles. We conclude that this dust component is directly associated with the FB

Table 1. Spectral synchrotron+dust model fit.

Bubble	Region ^a	α	ν_b	T
			GHz	K
North	Near	-0.88 ± 0.10	27.8 ± 14.4	30.0 ± 0.8
	Mid	-0.59 ± 0.08	24.8 ± 9.7	27.8 ± 0.5
	Far	-0.59 ± 0.06	23.6 ± 7.2	29.6 ± 0.4
South	Near	-0.78 ± 0.03	34.7 ± 12.5	31.5 ± 0.9
	Mid	-0.80 ± 0.03	29.3 ± 8.6	33.9 ± 0.8
	Far	-0.75 ± 0.02	37.4 ± 7.6	32.5 ± 0.5

^aThe downstream regions are defined in Fig. 3; in north bubble regions, $\nu < \text{GHz}$ data were excluded from the fit due to interfering substructure.

shock, probably due to dust entrainment or formation in the postshock region, in resemblance of AGB stars, novae, and core-collapse supernovae. Indeed, Fig. 2 shows some of the dust emission (green and blue) extending to the top of the γ -ray (red) bubbles. A dust FB component should therefore be included in template analyses that aim at measuring the microwave spectrum.

5. Joint bulk and edge model

The unexpected, hard microwave dust-emission downstream explains in part why a cooling break was not identified until now. Indeed, Fig. 3 shows that if the dust model is subtracted from the data, the remaining synchrotron component (dashed curves) presents a spectral break (insets) around ~ 35 GHz, as anticipated above. In accordance, fitting a superposition of synchrotron emission of index α and a frequency ν_b cooling break, and thermal dust emission of temperature T , as summarized in Table 1, gives $\nu_b = 34 \pm 5$ GHz in the southern bubble. Curiously, both *WMAP* (Dobler 2012b) and joint *WMAP* and *Planck* (Planck Collaboration 2013) template-based analyses found a similar bulk spectral break in the total synchrotron signal, but attributed it to combined hard+soft foregrounds rather than to the bubbles.

With this spectral break, solving Eqs. (4)–(7) in the downstream region, where $p = 1 - 2\alpha \simeq 2.5$, yields

$$t \simeq 5.2 \varepsilon_1^{-3/2} \left(\frac{\epsilon_{b,3}}{\nu_{b,35}} \right)^{7/4} \frac{u_s}{u} \Phi_{0.2} \text{ Myr}, \quad (9)$$

$$u_s \simeq 2.5 \varepsilon_1^2 \epsilon_{b,3}^{-9/4} \nu_{b,35}^{7/4} \Phi_{0.2}^{-1} \text{ eV cm}^{-3}, \quad (10)$$

$$B \simeq 4.2 \varepsilon_1 \epsilon_{b,3}^{-1} \nu_{b,35} \mu\text{G}, \quad (11)$$

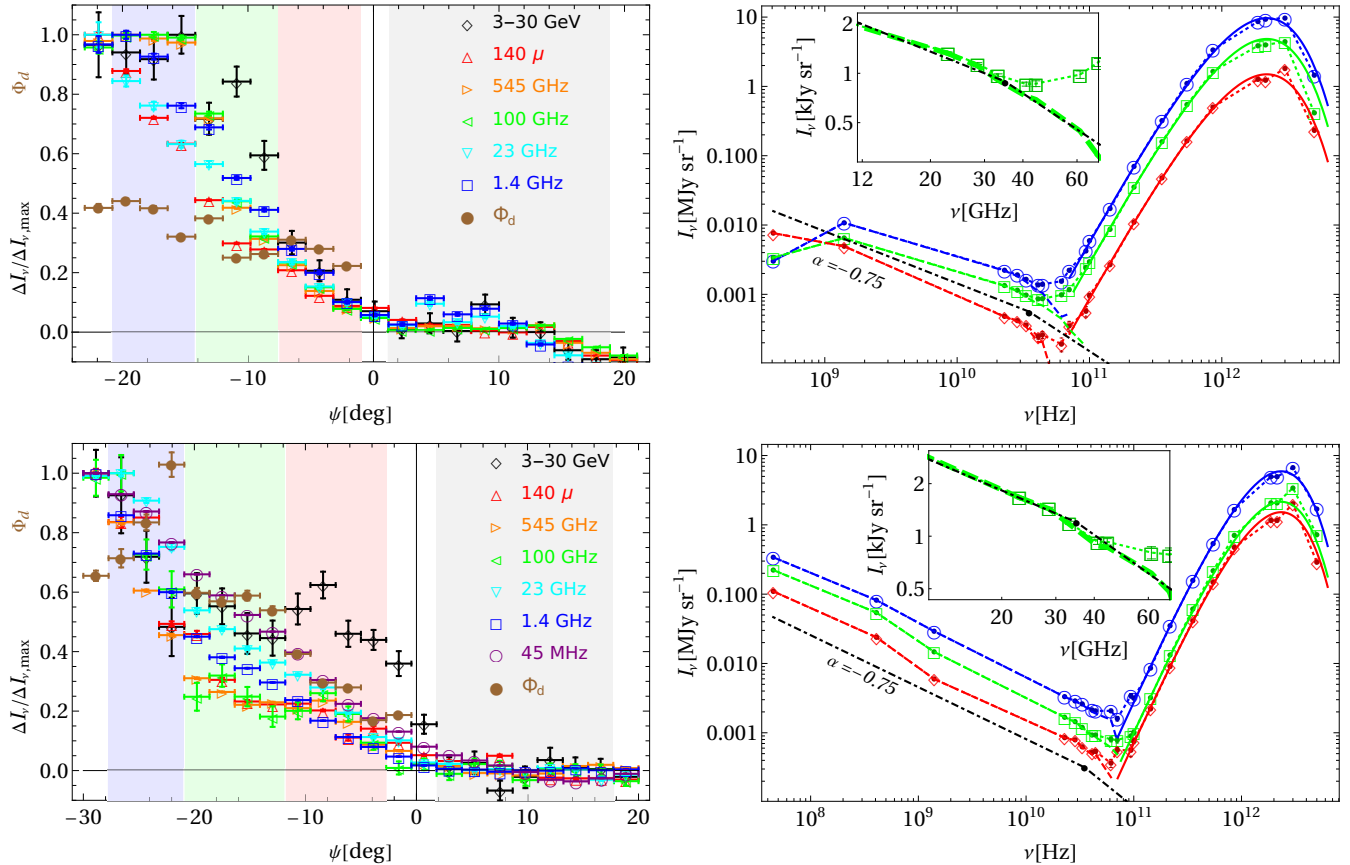


Figure 3. Spectral analysis of north (top panels) and south (bottom) FB edges. Left panels show (error bars) the profiles of select (see legend) channels (normalized by their maxima) and the 23 GHz to 10 GeV brightness ratio Φ_d , as a function of the angular distance ψ from the edge, after subtracting the foreground based on the upstream ($\psi > 0$) gray-shaded region. Right panels show (symbols enclosing error bars, with dotted lines to guide the eye) the spectrum of excess emission in the near (red diamonds), mid (green squares), and far (blue circles) downstream regions designated by the respective color-shaded regions in the left panels. Also shown are the synchrotron profiles (dashed curves) obtained by subtracting the respective best-fitted dust models (see text; solid curves) from the downstream excess, and a synchrotron model (of arbitrary normalization; labeled dot-dashed black) of $p = 2$ CRE injection, Kraichnan diffusion, and a $\nu_b = 35$ GHz cooling break (black disk); the insets focus on the cooling-break region in the mid-downstream. Data are extracted from 45 MHz (Alvarez et al. 1997; Maeda et al. 1999), reprocessed 408 MHz (Haslam et al. 1982; Remazeilles et al. 2015), 1.4 GHz (Reich 1982; Reich & Reich 1986; Reich et al. 2001), *WMAP* and *Planck* microwave, 160 μm and 140 μm AKARI (Doi et al. 2015), 100 μm and 60 μm IRIS (Miville-Deschênes & Lagache 2005), and 3–30 GeV *Fermi*-LAT maps.

and

$$u/u_s = 1 + 0.17(\epsilon_{b,3}\nu_{b,35})^{1/4}\Phi_{0.2}, \quad (12)$$

where we defined $\nu_{b,35} \equiv \nu_b/35$ GHz and a downstream $\Phi_{0.2} \equiv \Phi_d/0.2$ (see Fig. 3). While $\Phi_d \simeq 0.2$ remains fairly uniform in the north, it increases inward beyond $\psi \sim -10^\circ$ in the south; however, our method is increasingly sensitive to foreground variations at large $|\psi|$.

While the local spectral measurement near the edge does not require strong assumptions concerning extended foregrounds, and does not suffer from template-removal systematics (Keshet & Gurwicz 2017, 2018) which can be highly detrimental (*e.g.*, Keshet et al. 2004), it does show larger statistical errors than the volume-integrated, bulk spectrum. Our results indicate that this bulk spectrum too must show a cool-

ing break, which would fix the FB parameters even without using the hydrodynamic Eq. (2). Requiring similar FB ages inferred from edge and bulk spectra suggests a $\nu_{\text{bulk}} \simeq 23$ GHz cooling break in the latter, unidentified so far due to modelling systematics and unaccounted FB dust. We then obtain for the bulk $t \simeq 5.2\varepsilon_1^{-3/2}(\epsilon_{b,3}/\nu_{b,23})^{1.55}(u_s/u)\Phi_{0.1}$ Myr, $u_s \simeq 2.5\varepsilon_1^2\epsilon_{b,3}^{-2.05}\nu_{b,23}^{1.55}\Phi_{0.1}^{-1}$ eV cm $^{-3}$, $u/u_s \simeq 1 + 0.077\nu_{b,23}^{0.45}\Phi_{0.1}$, and

$$B \simeq 2.8\varepsilon_1\epsilon_{b,3}^{-1}\nu_{b,23}\mu\text{G}, \quad (13)$$

where we defined $\nu_{b,23} \equiv \nu_{\text{bulk}}/23$ GHz. Note that while a $\nu_{\text{bulk}} < 60$ GHz cooling break would modify the previously reported $\alpha \simeq 0.55$ synchrotron spectrum, a $p \simeq 2.1$ CRE spectrum is nevertheless needed for a self-

consistent model, as well as for an acceptable γ -ray fit (see Appendix A).

6. Discussion

We conclude that the spectra of both north and south FB edges, and of the bulk, both with and without hydrodynamic considerations, produce consistent results, thus providing strong constraints on the FBs and their environment. The results indicate younger FBs than obtained in early spectral models, an enhanced magnetic field near the edges, and strong and fairly uniform radiation fields throughout the bubbles. Indeed, while we cannot directly measure the ambient starlight intensity, Fig. 3 shows an infrared $\nu u_\nu \simeq 0.1 \text{ eV cm}^{-3}$ peak at high-latitudes, very similar to its estimated value near the Galactic plane (*e.g.*, $\nu u_\nu \simeq 0.15 \text{ eV cm}^{-3}$ at $R = 2 \text{ kpc}$; Ackermann et al. 2014).

The success of our oversimplified, one-zone bulk model, which attributes the synchrotron and IC signals to the same pure power-law CRE injection, in-

validates the justification for previous hadronic or leptonic models, which invoked ad-hoc cutoffs on the CR spectrum. Without ad-hoc assumptions, future better measurements of the broadband, radio to γ -ray signal would robustly constrain the CRE distribution and diffusion, coincident radiation fields, magnetic fields, and FB dynamics and energetics. The edge spectra presented in this work validate the bulk model, directly confirming the CRE softening expected from diffusion (Keshet & Gurwich 2017), the anticipated microwave cooling break, and, indirectly, the persistence of strong radiation fields throughout the FBs.

We thank K.C. Hou, O. Freifeld, E. Waxman, and R. Crocker for useful discussions. This research was supported by the Israel Science Foundation (Grant No. 2126/22), by the IAEC-UPBC joint research foundation (Grant No. 300/18), and by the Ministry of Science, Technology & Space, Israel.

APPENDIX

A. Leptonic model

In our one-zone leptonic model, FB γ -ray emission is dominated by the IC scattering of starlight. For simplicity, we approximate the integrated CR population as injected at a constant rate, so its evolved spectrum is a simple broken power-law. Equations (3)–(7) follow directly (*e.g.*, Rybicki & Lightman 1979), where the dimensionless prefactor

$$\begin{aligned} \phi &\equiv \frac{2^{\frac{3}{2}} \pi^{\frac{3p+2}{2}} (6+p)(4+p) \Gamma\left(\frac{p}{4} - \frac{1}{12}\right) \Gamma\left(\frac{19}{12} + \frac{p}{4}\right) \Gamma\left(\frac{p+1}{4}\right)}{3^2 80^{\frac{p}{2}} (16+6p+p^2) \Gamma\left(\frac{p+2}{2}\right) \Gamma\left(\frac{7+p}{4}\right) \zeta\left(\frac{6+p}{2}\right) \zeta(3)^{\frac{p-2}{2}}} \\ &\simeq 30.5 \times 2.7^{-1.6p} \text{ (approximation for } 2 < p < 3) \end{aligned} \quad (\text{A1})$$

of the ratio Φ between non-cooled synchrotron and cooled IC spectra is obtained after averaging over photons in a seed distribution of temperature T ,

$$\epsilon_0 \equiv \langle \epsilon \rangle_T = \frac{\pi^4 k_B T}{30 \zeta(3)} \simeq 2.7 k_B T, \quad (\text{A2})$$

and averaging the pitch angle α over an isotropic distribution,

$$\langle \sin(\alpha)^{\frac{p+1}{2}} \rangle = \frac{\pi^{\frac{1}{2}} \Gamma\left(\frac{p+5}{4}\right)}{2 \Gamma\left(\frac{p+7}{4}\right)} \simeq \frac{14}{17} - \frac{p}{19}, \quad (\text{A3})$$

approximated for $2 < p < 3$. Here, $\zeta(s)$ is the Riemann Zeta function and $\Gamma(z)$ is the Euler gamma function. Our numerical spectral computations, incorporating the

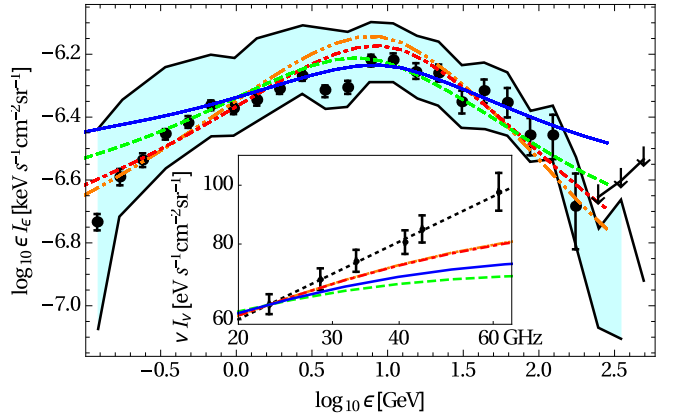


Figure 4. Same as Fig. 1, but for $p = 2$ and model parameters $\{u_s \text{ cm}^3/\text{eV}, t/\text{Myr}, B/\mu\text{G}\} = \{0.5, 10, 1.7\}$ (solid blue), $\{1, 8, 2\}$ (dashed green), $\{2, 3.6, 2.6\}$ (dot-dashed red), and $\{3, 2.7, 3\}$ (double-dot-dashed orange).

KN suppression, follow Refs. (Jones 1968; Aharonian & Atoyan 1981); results are shown for $p = 2.0$ and $p = 2.2$ in Figs. 4 and 5. For $p \gtrsim 2.3$, the γ -ray fit becomes increasingly worse and requires unreasonably young FBs and intense starlight, as illustrated in Figs. 6 and 7.

B. Microwave sky maps

We combine *Planck* mission and *Wilkinson Microwave Anisotropy Probe* (*WMAP*) data to produce the microwave maps for the analysis. We use the full mission, bandpass-leakage corrected, 28.5, 44.1, 70.3, 100.0, and

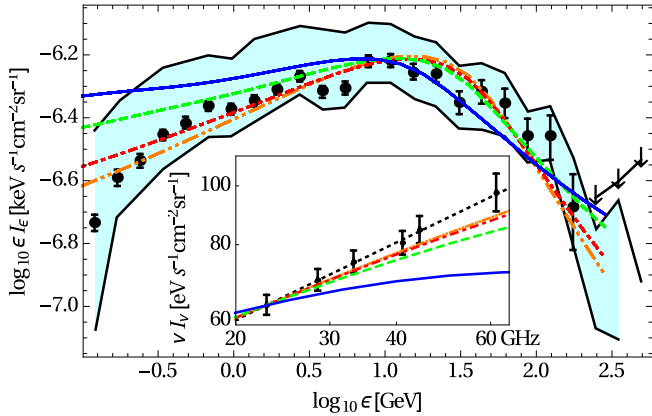


Figure 5. Same as Fig. 1, but for $p = 2.2$ and model parameters $\{u_s \text{ cm}^3/\text{eV}, t/\text{Myr}, B/\mu\text{G}\} = \{0.5, 8, 1.45\}$ (solid blue), $\{1, 3.2, 2\}$ (dashed green), $\{2, 1.6, 2.8\}$ (dot-dashed red), and $\{3, 1.1, 3.4\}$ (double-dot-dashed orange).

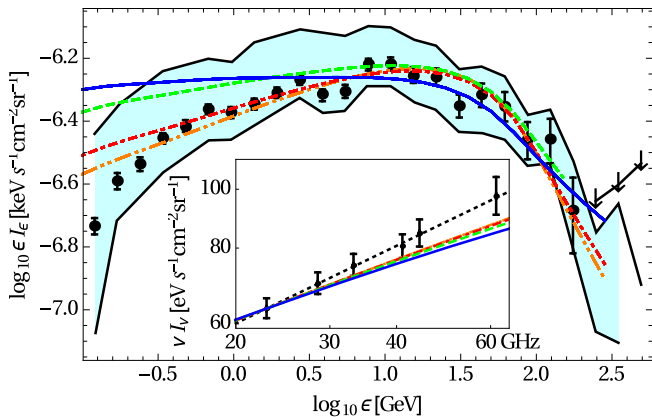


Figure 6. Same as Fig. 1, but for $p = 2.3$ and model parameters $\{u_s \text{ cm}^3/\text{eV}, t/\text{Myr}, B/\mu\text{G}\} = \{0.5, 3.3, 1.7\}$ (solid blue), $\{1, 1.8, 2.1\}$ (dashed green), $\{2, 1, 2.9\}$ (dot-dashed red), and $\{3, 0.7, 3.5\}$ (double-dot-dashed orange).

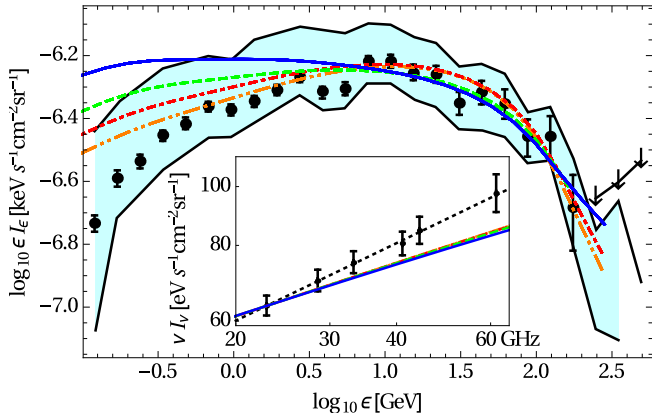


Figure 7. Same as Fig. 1, but for $p = 2.4$ and model parameters $\{u_s \text{ cm}^3/\text{eV}, t/\text{Myr}, B/\mu\text{G}\} = \{0.5, 2.2, 1.7\}$ (solid blue), $\{1, 1.2, 2.2\}$ (dashed green), $\{2, 0.7, 2.8\}$ (dot-dashed red), and $\{3, 0.5, 3.4\}$ (double-dot-dashed orange).

143.0 GHz maps from *Planck*³, and the nine-year, deconvolved maps of the 22.8, 33.2, 41.0, 61.4, and 94.0 GHz bands from *WMAP*⁴.

Binning along the FB edge removes most foregrounds, but to obtain better results, we first subtract the CMB contribution, estimated using the Planck HFI internal linear combination (PILC; Planck Collaboration 2013). This map is constructed by a superposition of 143–545 GHz maps, designed to spectrally isolate the CMB from the dust template of Finkbeiner et al. (1999).

We mask the point sources from *WMAP*'s nine-year point-source catalog and *Planck*'s second catalogue of point sources (PCCS2) in the relevant bands, and the following large-scale structures: the Small and Large Magellanic Clouds, M31, NGC5090, NGC5128, Orion-Barnard Loop, and ζ Oph. We also mask pixels where dust extinction at $H\alpha$ frequencies is larger than 1 mag, and pixels where the $H\alpha$ intensity is greater than 10 Rayleigh. All maps are masked at the highest, $N_{\text{side}} = 2048$ HEALPix (Górski et al. 2005) resolution available.

C. Fermi-LAT sky map

We use the archival Pass-8 LAT data from the Fermi Science Support Center (FSSC)⁵, and the Fermi Science Tools (version v10r0p5). Weekly all-sky files are used, spanning weeks 9 through 789 for a total of 781 weeks (~ 15 years), with ULTRACLEANVETO class photon events. A 90° zenith angle cut is applied to avoid CR-generated γ -rays from the Earth's atmospheric limb, according to the appropriate FSSC Data Preparation recommendations. Good time intervals are selected using the recommended expression (`DATA_QUAL==1`) and (`LAT_CONFIG==1`). Point-source contamination is minimized by masking pixels within the 95% total-event containment area of each point source in the LAT fourth source catalog (4FGL; Abdollahi et al. 2020).

REFERENCES

- Abdollahi, S., Acero, F., Ackermann, M., et al. 2020, *ApJS*, 247, 33, doi: [10.3847/1538-4365/ab6bcb](https://doi.org/10.3847/1538-4365/ab6bcb)
- Ackermann, M., Albert, A., Atwood, W. B., et al. 2014, *ApJ*, 793, 64, doi: [10.1088/0004-637X/793/1/64](https://doi.org/10.1088/0004-637X/793/1/64)
- Aharonian, F. A., & Atoyan, A. M. 1981, *Ap&SS*, 79, 321, doi: [10.1007/BF00649428](https://doi.org/10.1007/BF00649428)
- Ajello, M., Albert, A., Atwood, W. B., et al. 2016, *ApJ*, 819, 44, doi: [10.3847/0004-637X/819/1/44](https://doi.org/10.3847/0004-637X/819/1/44)
- Alvarez, H., Aparici, J., May, J., & Olmos, F. 1997, *A&AS*, 124, 205, doi: [10.1051/aas:1997196](https://doi.org/10.1051/aas:1997196)
- Axford, W. I., Leer, E., & Skadron, G. 1977, in *International Cosmic Ray Conference*, Vol. 11, *International Cosmic Ray Conference*, 132–137
- Baganoff, F. K., Maeda, Y., Morris, M., et al. 2003, *ApJ*, 591, 891, doi: [10.1086/375145](https://doi.org/10.1086/375145)
- Bell, A. R. 1978, *MNRAS*, 182, 147
- Berezinskii, V. S., Bulanov, S. V., Dogiel, V. A., & Ptuskin, V. S. 1990, *Astrophysics of cosmic rays* (Amsterdam: North-Holland, 1990, edited by Ginzburg, V.L.)
- Bernstein, I. B., & Book, D. L. 1980, *ApJ*, 240, 223, doi: [10.1086/158226](https://doi.org/10.1086/158226)
- Bland-Hawthorn, J., & Cohen, M. 2003, *ApJ*, 582, 246, doi: [10.1086/344573](https://doi.org/10.1086/344573)
- Blandford, R. D., & Ostriker, J. P. 1978, *ApJL*, 221, L29, doi: [10.1086/182658](https://doi.org/10.1086/182658)
- Courant, R., & Friedrichs, K. O. 1948, *Supersonic flow and shock waves*
- Crocker, R. M., & Aharonian, F. 2011, *Physical Review Letters*, 106, 101102, doi: [10.1103/PhysRevLett.106.101102](https://doi.org/10.1103/PhysRevLett.106.101102)
- Dobler, G. 2012a, *ApJL*, 760, L8, doi: [10.1088/2041-8205/760/1/L8](https://doi.org/10.1088/2041-8205/760/1/L8)
- . 2012b, *ApJ*, 750, 17, doi: [10.1088/0004-637X/750/1/17](https://doi.org/10.1088/0004-637X/750/1/17)
- Dobler, G., Finkbeiner, D. P., Cholis, I., Slatyer, T., & Weiner, N. 2010, *ApJ*, 717, 825, doi: [10.1088/0004-637X/717/2/825](https://doi.org/10.1088/0004-637X/717/2/825)
- Doi, Y., Takita, S., Ootsubo, T., et al. 2015, *PASJ*, 67, 50, doi: [10.1093/pasj/psv022](https://doi.org/10.1093/pasj/psv022)
- Finkbeiner, D. P. 2004, *ApJ*, 614, 186, doi: [10.1086/423482](https://doi.org/10.1086/423482)
- Finkbeiner, D. P., Davis, M., & Schlegel, D. J. 1999, *ApJ*, 524, 867, doi: [10.1086/307852](https://doi.org/10.1086/307852)
- Fujita, Y., Ohira, Y., & Yamazaki, R. 2013, *ApJL*, 775, L20, doi: [10.1088/2041-8205/775/1/L20](https://doi.org/10.1088/2041-8205/775/1/L20)
- Górski, K. M., Hivon, E., Banday, A. J., et al. 2005, *ApJ*, 622, 759, doi: [10.1086/427976](https://doi.org/10.1086/427976)
- Haslam, C. G. T., Salter, C. J., Stoffel, H., & Wilson, W. E. 1982, *A&AS*, 47, 1
- Hooper, D., & Slatyer, T. R. 2013, *Physics of the Dark Universe*, 2, 118, doi: [10.1016/j.dark.2013.06.003](https://doi.org/10.1016/j.dark.2013.06.003)
- Huang, W.-C., Urbano, A., & Xue, W. 2013, *ArXiv e-prints*. <https://arxiv.org/abs/1307.6862>
- Jones, F. C. 1968, *Physical Review*, 167, 1159, doi: [10.1103/PhysRev.167.1159](https://doi.org/10.1103/PhysRev.167.1159)
- Kataoka, J., Tahara, M., Totani, T., et al. 2013, *ApJ*, 779, 57, doi: [10.1088/0004-637X/779/1/57](https://doi.org/10.1088/0004-637X/779/1/57)
- Keller, J. B. 1956, *Quarterly of Applied Mathematics*, 14 No. 2, 171
- Keshet, U., Arad, O., & Lyubarski, Y. 2020, *ApJ*, 891, 117, doi: [10.3847/1538-4357/ab765e](https://doi.org/10.3847/1538-4357/ab765e)
- Keshet, U., & Gurwich, I. 2017, *ApJ*, 840, 7, doi: [10.3847/1538-4357/aa6936](https://doi.org/10.3847/1538-4357/aa6936)
- . 2018, *MNRAS*, 480, 223, doi: [10.1093/mnras/sty1533](https://doi.org/10.1093/mnras/sty1533)
- Keshet, U., Waxman, E., & Loeb, A. 2004, *JCAP*, 4, 6, doi: [10.1088/1475-7516/2004/04/006](https://doi.org/10.1088/1475-7516/2004/04/006)
- Kraichnan, R. H. 1965, *Physics of Fluids*, 8, 1385, doi: [10.1063/1.1761412](https://doi.org/10.1063/1.1761412)
- Krymskii, G. F. 1977, *Akademiia Nauk SSSR Doklady*, 234, 1306
- Maeda, K., Alvarez, H., Aparici, J., May, J., & Reich, P. 1999, *A&AS*, 140, 145, doi: [10.1051/aas:1999413](https://doi.org/10.1051/aas:1999413)
- Miller, M. J., & Bregman, J. N. 2013, *ApJ*, 770, 118, doi: [10.1088/0004-637X/770/2/118](https://doi.org/10.1088/0004-637X/770/2/118)
- Miville-Deschênes, M.-A., & Lagache, G. 2005, *ApJS*, 157, 302, doi: [10.1086/427938](https://doi.org/10.1086/427938)
- Mondal, S., Keshet, U., Sarkar, K. C., & Gurwich, I. 2022, *MNRAS*, 514, 2581, doi: [10.1093/mnras/stac1084](https://doi.org/10.1093/mnras/stac1084)
- Planck Collaboration. 2013, *A&A*, 554, A139, doi: [10.1051/0004-6361/201220271](https://doi.org/10.1051/0004-6361/201220271)
- Planck Collaboration, Aghanim, N., Ashdown, M., et al. 2016, *A&A*, 596, A109, doi: [10.1051/0004-6361/201629022](https://doi.org/10.1051/0004-6361/201629022)
- Popescu, C. C., Yang, R., Tuffs, R. J., et al. 2017, *MNRAS*, 470, 2539, doi: [10.1093/mnras/stx1282](https://doi.org/10.1093/mnras/stx1282)
- Reich, P., & Reich, W. 1986, *A&AS*, 63, 205
- Reich, P., Testori, J. C., & Reich, W. 2001, *A&A*, 376, 861, doi: [10.1051/0004-6361:20011000](https://doi.org/10.1051/0004-6361:20011000)
- Reich, W. 1982, *A&AS*, 48, 219
- Remazeilles, M., Dickinson, C., Banday, A. J., Bigot-Sazy, M.-A., & Ghosh, T. 2015, *MNRAS*, 451, 4311, doi: [10.1093/mnras/stv1274](https://doi.org/10.1093/mnras/stv1274)
- Rybicki, G. B., & Lightman, A. P. 1979, *Radiative processes in astrophysics*

³ See <https://pla.esac.esa.int/#home>

⁴ See https://lambda.gsfc.nasa.gov/product/map/dr5/maps_deconv_band_r9_i_9yr_get.cfm

⁵ See <http://fermi.gsfc.nasa.gov/ssc>

Sarkar, K. C., Mondal, S., Sharma, P., & Piran, T. 2023, ApJ, 951, 36, doi: [10.3847/1538-4357/acd75d](https://doi.org/10.3847/1538-4357/acd75d)
Sherf, N., Keshet, U., & Gurwich, I. 2017, ApJ, 847, 95, doi: [10.3847/1538-4357/aa894f](https://doi.org/10.3847/1538-4357/aa894f)
Su, M., Slatyer, T. R., & Finkbeiner, D. P. 2010, ApJ, 724, 1044, doi: [10.1088/0004-637X/724/2/1044](https://doi.org/10.1088/0004-637X/724/2/1044)

Yang, H.-Y. K., Ruszkowski, M., & Zweibel, E. 2013, MNRAS, doi: [10.1093/mnras/stt1772](https://doi.org/10.1093/mnras/stt1772)